

# NUMERICAL STUDY OF NON-GYROTROPIC ELECTRON PRESSURE EFFECTS IN MAGNETIC RECONNECTION

A. Sladkov,<sup>1</sup> R. Smets,<sup>2</sup> N. Aunai,<sup>2</sup> and A. Korzhimanov<sup>1</sup>

<sup>1</sup>*Institute of Applied Physics, 46 Ulyanov Street, 603950 Nizhny Novgorod, Russia*

<sup>2</sup>*Lab. Phys. Plasmas, Sorbonne Universités, 4 place Jussieu, F-75252 Paris, France*

We investigate time evolution of six-component electron pressure tensor in a hybrid code studying consequences for the two-dimensional reconnection process in a modified Harris sheet. We put forward that two tensor components (a diagonal and a non-diagonal one) grow in an unstable way unless an isotropization operator is considered. This isotropization term is physically associated with an electron heat flux. As a consequence, we put forward that an enhanced value of a diagonal component is observed in the very middle of field reversal at electron scale. To ensure pressure balance the magnetic field is decreased in this electron layer, increasing the associated out-of-plane current at its edges. The bifurcation mechanism is based on the presence of electron pressure anisotropy, related to the gradient of inflow bulk velocity of electrons. Particles entering the X-point region experience drag forces, resulting from electron pressure gradient in inflow direction. We suggest that smaller reconnection rate for double-peaked current sheets comparing with single-peaked is a consequence of this bifurcation.

## I. INTRODUCTION

Magnetic reconnection is well known to be an ubiquitous plasma process, occurring in laboratory<sup>1</sup>, space<sup>2</sup> and astrophysical<sup>3</sup> plasmas. It has been widely studied as it is an important transport and energy conversion process. While in nature reconnection could be very unsteady, many numerical simulations of a single X point developing in a two-dimensional Harris sheet suggested a nearly stationary process<sup>4</sup> after the onset. It essentially results from the fixed-size computational domain, the limited number of particles and the uniform upstream plasma. While artificial, such setups then allow to quantitatively investigate the reconnection process during this stationary phase.

The out-of-plane component of the electric field is crucial in studying two-dimensional magnetic reconnection as this term quantifies the rate at which magnetic flux is transported in and out from the reconnection region. Upstream of the reconnection region, the out-of-plane component of electric field is essentially due to  $\mathbf{V}_i \times \mathbf{B}$  term, which is associated with the ions, drifting at velocity  $\mathbf{V}_i$  in the magnetic field  $\mathbf{B}$ . Approaching the mid-plane of the current sheet, this term vanishes because both the magnetic field and the ion velocity vanish (the ions being demagnetized). It is known<sup>5</sup> that the out-of-plane electric field is sustained by the Hall term in the so-called ion diffusion region, while in the electron diffusion region, the electron pressure term<sup>6</sup> seems to be dominant.

In his pioneering work, Vasyliunas<sup>7</sup> pointed out the importance of non-gyrotropic electron pressure tensor, as being able to account for out-of-plane component of the electric field at the stagnation point. Different numerical works on symmetric reconnection have already shown that non-gyrotropic contribution to the reconnection electric field exceeds the corresponding bulk flow inertial contribution<sup>8,9</sup>. The divergence of electron pressure tensor is hence the main term for the out-of-plane

electric field. Non-diagonal terms of the pressure tensor naturally result from the non-gyrotropy of associated distribution function<sup>6</sup>. In full-PIC codes, such effects are well-captured, but often at the cost of huge CPU time<sup>10</sup> and/or unrealistic mass ratio and/or small physical domains. An alternative is to treat electrons as a fluid, like in hybrid or two-fluid codes.

In collisionless plasmas, the time evolution of six-component electron pressure tensor contains three terms. We remind here the form introduced by Winske<sup>11</sup> using index notation :

$$\begin{aligned} \partial_t P_{ij} = & -v_k \partial_k P_{ij} - P_{ij} \partial_k v_k - P_{ik} \partial_k v_j - P_{jk} \partial_k v_i \\ & - \frac{e}{m_e} [P_{ik} B_n \varepsilon_{knj} + P_{jk} B_n \varepsilon_{kni}] \\ & - \partial_k Q_{ijk} \end{aligned} \quad (1)$$

where  $\varepsilon_{knj}$  is the Levi-Civita symbol. Following the terminology of Hesse<sup>12</sup>, the driver term  $[D]$  (first line of right hand side of Eq. (1) is associated with the transport of pressure at the electron fluid velocity  $v$ , the cyclotron term  $[C]$  (second line) is associated with the rotation of pressure at the electron gyrofrequency, and the divergence of electron heat flux (third line), usually replaced by isotropization term  $[I]$ . As a consequence, resolving Eq. (1) requires to correctly treat the time integration of the term  $[C]$  at electron scale, but also to find an appropriate form for the term  $[I]$ . In this work, we call  $X$  the field reversal direction,  $Y$  the gradient direction for both magnetic field magnitude and density, and  $Z$  the direction of current associated with the field reversal.

The first numerical study<sup>11</sup> investigating the time-evolution of electron pressure tensor only considered the terms  $[D]$  and  $[I]$ , assuming that the term  $[C]$  also results in an isotropization process. That numerical study<sup>11</sup> already outlined the importance of the term  $[I]$  in order to limit the size of off-diagonal elements of the electron pressure tensor. The same problem has been revisited<sup>12</sup>

including the term  $[C]$ , numerically treated in an implicit way in order to remove the time step constraint resulting from the electron mass (the cyclotron term linearly depends on the electron gyrofrequency).

In this study, we present an explicit method for the time integration of evolution equation of the six-component electron pressure tensor in a hybrid code, and discuss the importance of electron heat flux acting as a regularizing term on each of the components of this tensor. In section II, we introduce the hybrid numerical model. In section III, we give details for the numerical integration of the electron pressure tensor. In section IV, we display the structures of components of the pressure tensor and discuss their origin. In section V we discuss the macroscopic consequences of regularizing the  $P_{xx}$  and  $P_{xy}$  components for the current sheet structure at electron scale. Section VI is dedicated to discuss the consequences for reconnection process.

## II. NUMERICAL MODEL

In this work, electrons are described in a fluid way, by their three first moments : density, bulk velocity and the six-component pressure tensor (pressure tensor being symmetric, by definition). To properly describe the decoupling of ions from the magnetic field in ion diffusion region, we keep the ions description at the particle level. Hence, we use a hybrid code<sup>13</sup>.

The displacement current is neglected as the phase velocity of electromagnetic fluctuations is small compared to the speed of light. We then need an electron Ohm's law :

$$\mathbf{E} = -\mathbf{V}_i \times \mathbf{B} + \frac{1}{en}(\mathbf{J} \times \mathbf{B} - \nabla \cdot \mathbf{P}_e) - \nu \Delta \mathbf{J} \quad (2)$$

In Eq. (2),  $\mathbf{V}_i$  is the ion bulk velocity,  $n$  is the electron density (equal to the total ion density by quasi-neutrality),  $\mathbf{J}$  is the total current density equal to the curl of  $\mathbf{B}$ ,  $\mathbf{P}_e$  is the electron pressure tensor and  $\nu$  is the hyper-viscosity. For the hyper-viscous term, we set  $\nu = 10^{-3}$ : while it provides a dissipation process at sub-ion scales, it is still smaller than the contribution of electron pressure tensor, at whatever scale, for the reconnection process.

The magnetic field and the density are normalized to their asymptotic values  $B_0$  and  $n_0$  respectively, lengths are normalized to the ion inertial length  $d_0$  (calculated using the density  $n_0$ ), times are normalized to the inverse of ion gyrofrequency  $\Omega_0^{-1}$  (calculated using the magnetic field  $B_0$ ) and velocities are normalized to the Alfvén velocity  $V_0$  (calculated using  $B_0$  and  $n_0$ ). The mass of ions and the charge, both equal 1. The normalization of the other quantities follows from these ones.

Electromagnetic fields are calculated on two staggered grids using a predictor-corrector scheme<sup>14</sup> in order to ensure a second order scheme. Ions dynamics is solved using a first order interpolation of the electromagnetic field<sup>15</sup>.

At each time step, the particle moments, namely the density and the velocity, are computed in each cell using a first order assignment function for each macro-particles. These ion moments are smoothed using a three-points stencil. Such smoothing helps to prevent the growth of small-scale electric fields in low-density areas and has limited consequences for the numerical diffusion processes.

We use a Harris sheet<sup>16</sup> as an initial condition for which  $\mathbf{B}(y) = B_0 \tanh(y/\lambda)\hat{\mathbf{x}}$  and  $n(y) = n_0 \cosh^{-2}(y/\lambda)$ . Such a kinetic equilibrium is entirely defined by the temperature ratio  $T_i/T_e$ , equal to 1 in this study. We also include a background ion population, with uniform density  $n_b$  (equal to 0.5 in this study) and the same temperature as foreground ions forming the current sheet. A small initial magnetic perturbation<sup>17</sup> is superposed to the Harris equilibrium in the very middle of the box.

The simulation domain is rectangular with a length  $L_X = 102.4$  and a width  $L_Y = 20.8$ . We use a  $1024 \times 208$  grid corresponding to a mesh size equal to 0.1 in both directions. We initially set 40 millions of particles in this domain, meaning that initially, there are about 180 particles per cell in the lowest-density regions. The time-step is  $2 \times 10^{-4}$  in order to satisfy the CFL conditions for the fastest whistler modes. Each run lasts  $t_{\max} = 100 \Omega_0^{-1}$ . We use periodic boundary conditions in the  $X$  direction and perfect conducting boundaries in the  $Y$  direction as the magnetic field and density profiles are not periodic functions.

In the next section, we discuss the equation governing the time evolution of electron pressure tensor, the importance of each of its terms, and the way these terms can be numerically computed.

## III. SIX-COMPONENT ELECTRON PRESSURE TENSOR EQUATION

In most hybrid codes, the pressure is scalar and evolves through time in an isothermal way. Although simple, this hypothesis is generally hard to justify, and consequences for the reconnection process are yet unclear. Especially in 2D current sheet, as it does not support the reconnection electric field. Furthermore, the electron temperature has to be uniform, otherwise, the temperature gradient initially given would stay as is while transport processes generally act in a way to reduce such gradients. As we use the six-component pressure tensor equation, further we discuss each term on the right hand side of Eq. (1) in order to understand the underlying physical effects, as well as the associated numerical constraints.

The driver term is written

$$D(\mathbf{P}) = -\mathbf{V}_e \cdot \nabla \mathbf{P} - \mathbf{P} \nabla \cdot \mathbf{V}_e - \mathbf{P} \cdot \nabla \nabla \cdot \mathbf{V}_e - (\mathbf{P} \cdot \nabla \nabla \cdot \mathbf{V}_e)^T \quad (3)$$

where the electron bulk velocity  $\mathbf{V}_e$  is expressed through the ion bulk velocity and the current density :  $\mathbf{V}_e = \mathbf{V}_i - \mathbf{J}/n$ .

The four terms involved in  $D$  can be split in three parts :

- $D_A = -\mathbf{V}_e \cdot \nabla \mathbf{P}$  is the advection of electron pressure at the electron velocity. For such advection equation, we use the first order upwind scheme which is well designed
- $D_C = -\mathbf{P} \nabla \cdot \mathbf{V}_e$  is associated with the plasma compressibility. It is numerically integrated with an explicit first order space-centered scheme
- $D_S = -\mathbf{P} \cdot \nabla \mathbf{V}_e - (\mathbf{P} \cdot \nabla \mathbf{V}_e)^T$  is the symmetric part of the driver term and is also integrated with a first order space centered scheme

It is worth noticing that no electron time scales are present in these terms as the electron mass is not involved. Hence, no particular numerical constraints arise because of the time integration of these terms. A second important remark is that both  $D_A$  and  $D_C$  act on a  $P_{ij}$  component by only involving this same  $P_{ij}$  component. This is not the case for the  $D_S$  term, for which the time evolution of diagonal terms will depend on off-diagonal ones, and vice-versa. We will hence see that  $D_S$  is dominant term compared to  $D_A$  and  $D_C$ .

The cyclotron term is written

$$C(\mathbf{P}) = -\frac{e}{m}[\mathbf{P} \times \mathbf{B} + (\mathbf{P} \times \mathbf{B})^T] \quad (4)$$

This symmetrical term depends on the electron mass. Consequently, a constraint arises on the time step needed to integrate it. In a previous study<sup>12</sup>, this term was integrated in an implicit way resulting in the unconditionally stable numerical scheme. In our study, we develop a different numerical scheme using a sub-cycling technique. We also have an implementation of the implicit one for the purpose of comparison. These two methods converge to the same results, with about 30% of the total computational time saved using subcycling.

The last term of the right hand side of Eq. (1) is the divergence of electron heat flux. In the collisionless case the heat flux expression is a complex problem, as the equation for its time evolution is a heavy third order tensor equation involving the divergence of fourth order moment of the electron fluid. Hammett and Perkins<sup>18</sup> proposed an Ansatz form for the reduced heat flux which includes a set of free parameters. These parameters are defined such that the heat flux equals the third order moment of the first order distribution function (the zeroth order being a maxwellian) which is a solution of the Vlasov equation. This so-called Landau-fluid closure is well designed in a spectral representation as it is local in wave-number space, however it is non-local in real space. If considering a single dominant wave-number  $k_0$ , Wang et al.<sup>19</sup> proposed a simplified form :

$$\partial_k Q_{ijk} = k_0 v_T (P_{ij} - p \delta_{ij}) \quad (5)$$

where  $p = 1/3 \text{Tr}(\mathbf{P})$ , and  $v_T$  thermal velocity. As a consequence, this term essentially acts as an isotropization term for the electron pressure tensor.

A hybrid version of Eq. (1) therefore needs to choose a model for the heat flux divergence. The isotropization term we use

$$I(\mathbf{P}) = -\frac{1}{\tau}[\mathbf{P} - \frac{1}{3} \text{Tr}(\mathbf{P})] \quad (6)$$

In this form,  $\tau$  is the characteristic relaxation time scale. This isotropization term operates with the same efficiency for both diagonal and off-diagonal terms. We also emphasize that  $I_{ij}$  only depends on this  $ij$  component (no cross terms) except through the implicit relation in trace operation for the diagonal components.

The version of Eq. (1), that we use, is the following:

$$\begin{aligned} \partial_t \mathbf{P} = & -\mathbf{V}_e \cdot \nabla \mathbf{P} - \mathbf{P} \nabla \cdot \mathbf{V}_e - \mathbf{P} \cdot \nabla \mathbf{V}_e - (\mathbf{P} \cdot \nabla \mathbf{V}_e)^T \\ & - \frac{e}{m}[\mathbf{P} \times \mathbf{B} + (\mathbf{P} \times \mathbf{B})^T] \\ & - \frac{1}{\tau}[\mathbf{P} - \frac{1}{3} \text{Tr}(\mathbf{P})] \end{aligned} \quad (7)$$

The time step  $\Delta t$  we use for the equations is small enough to resolve the gyro-motion of ions. But the implemented sub-cycling method for explicit integration of the cyclotron term requires a smaller time step. Hence, defining  $\mu = m_i/m_e$  as the ion to electron mass ratio, a time step  $\Delta t/\mu$  is small enough to properly treat the electron magnetization. In this study we take  $\mu = 100$ , the electron inertial length  $d_e = 0.1 d_i$ . Because of time centering the electron pressure tensor is defined at half time step, advancing from  $P_{n-1/2}$  to  $P_{n+1/2}$  is done using  $\mu$  sub-cycles with the algorithm (for  $l \in [0, \mu - 1]$ )

$$\mathbf{P}_{n-\frac{1}{2}+\frac{l+1}{\mu}} = \mathbf{P}_{n-\frac{1}{2}+\frac{l}{\mu}} + \frac{\Delta t}{\mu} [C(\mathbf{P}_{n-\frac{1}{2}+\frac{l}{\mu}}) + D(\mathbf{P}_n) + I(\mathbf{P}_{n-\frac{1}{2}})] \quad (8)$$

The driver term is hence extrapolated at the predictor phase, and interpolated at the corrector one.

In this study, we discuss four types of runs, depending on the specific closure equation that is used. These types are labeled with tags (ranging from  $A$  to  $D$ ), which meanings are given in Table I. By default, we use  $\tau = 1$  for each case, unless the  $\tau$  value is explicitly given. In case  $D$ ,  $P_{xx}$  and  $P_{yy}$  are calculated using Eq. (7), but then are set to half of their sum in order to be used for the next time step. The anisotropy between the  $P_{xx}$  and  $P_{yy}$  terms is hence artificially quenched, while these terms are calculated with their appropriate time evolution equation.

In the next section we discuss results for run B, while runs C and D will be discussed and compared to run B in section V. Run A will be used for comparisons in both of sections IV and V.

| Run tag | Closure equation   |
|---------|--|
| A       | isothermal closure, scalar $P = nk_B T_0$                    |
| B       | tensor $\mathbf{P}$ (with subcycling for $[C]$ term)         |
| C       | tensor $\mathbf{P}$ with $[I]$ only on $P_{xx}$ and $P_{xy}$ |
| D       | tensor $\mathbf{P}$ with $P_{xx} = P_{yy}$                   |

TABLE I: Meaning of the four tags used for runs A, B, C and D.

#### IV. PHENOMENOLOGY OF THE SIX-COMPONENT ELECTRON PRESSURE TENSOR

The structure of diagonal components of the pressure tensor is discussed in the first part of this section, while the off-diagonal components are discussed in the second one. In each case, we distinguish two regions : the separatrix and the electron layer, a region close to the mid-plane  $Y = 0$ , at electron scale.

Panel (a) of Fig. 1 displays the  $P_{zz}$  component of the pressure tensor and shows a very clear structure of enhanced pressure in a thin and elongated layer close to the mid-plane  $Y = 0$ . This electron layer has a length between  $10 d_0$  and  $15 d_0$  and has a thickness smaller than the ion inertial length (that is at electron scale). While this thickness also depends on the location and on the time, we call it electron layer as this thickness is always at electron scale. Such electron layer has already been observed in both fully kinetic and two-fluid simulations<sup>19</sup>. Fully kinetic simulations of Harris-type magnetotail equilibrium showed that decreasing the electron mass down to realistic values resulted in decreased width of the non-gyrotropic region<sup>20</sup>.

We will show later that the increased  $P_{yy}$  in the mid-plane is accompanied by a decreased density, therefore it is consistent with the electrons heating in fully kinetic simulations<sup>6</sup>. Interestingly, the larger the isotropization term (replacing the divergence of electron heat flux), the thinner the electron layer. It emphasizes that the electron layer results from the anisotropy/agyrotropy of the electron pressure. In our case, this non-gyrotropy arises from interplay between all the terms in the pressure tensor evolution equation Eq. (7). In a model accounting for the kinetic nature of the electrons, such non-gyrotropy in the pressure tensor would arise from the non-gyrotropies of the underlying electron distribution functions, which themselves result from the non-adiabatic electron motion in electron scale regions.

Panels (b) and (c) of Fig. 1 display the difference of the  $P_{zz}$  component with the two other diagonal components of this tensor. Two very clear structures appear that outlines the anisotropy of the electrons :

- in the electron layer, the  $P_{yy}$  component is larger close to the  $X$  point (starting at  $X$  point until  $5 d_0$ ) and then gets smaller at the end of this electron layer

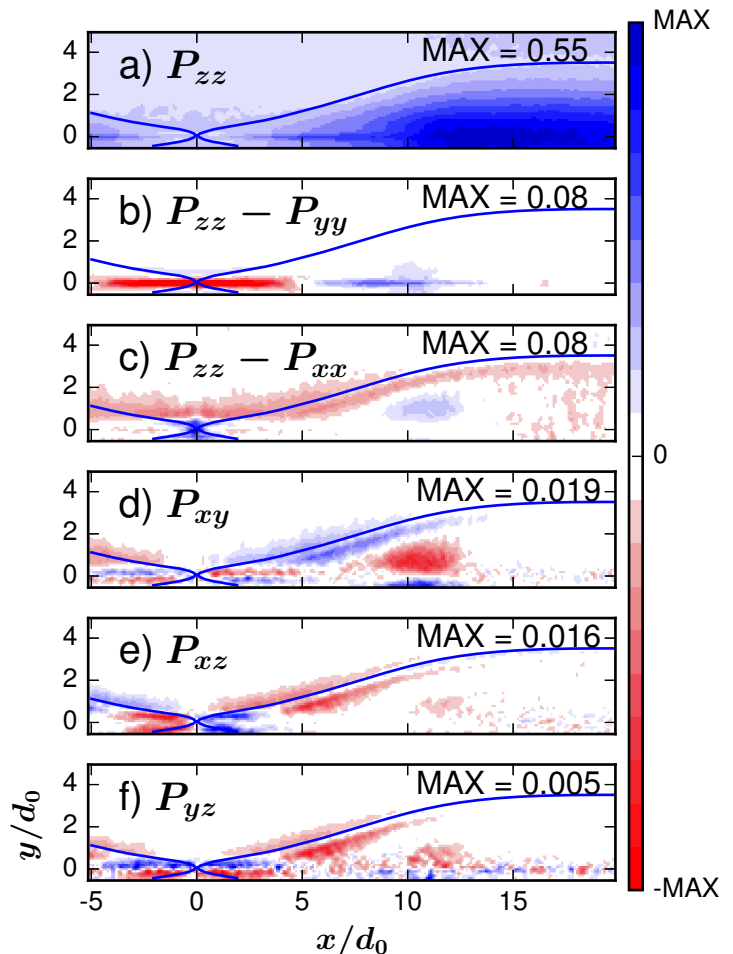


FIG. 1: Run B. (a) Diagonal component of the electron pressure tensor  $P_{zz}$ , (b) difference  $P_{zz} - P_{yy}$ , (c) difference  $P_{zz} - P_{xx}$ , (d)-(f) off-diagonal components at  $t = 80 \Omega_0^{-1}$ . For each panel the respective maximum values are indicated in frame. The separatrices are indicated in blue lines.

- on the separatrices, the  $P_{xx}$  component gets larger than  $P_{zz}$  (and  $P_{yy}$ ).

To clarify these features, we focus on the relative importance of the terms governing the time evolution of six-component electron pressure tensor.

Fig. 2 displays terms controlling time evolution of the  $P_{yy}$  component: the only non-negligible term in  $[Ds]$  (red), two terms in  $[C]$  (green and blue) and  $[I]$  (magenta). These values are averaged over 3 consecutive steps (namely 79.9, 80.0 and 80.1) in order to remove fluctuating nature of the terms. Solid lines are used when the associated term increases the absolute value of pressure component while dashed lines are used when this term decreases its absolute value. In the electron layer the picture is pretty clear, and exhibit a strong enhancement of the  $P_{yy}$  component. As a consequence, an anisotropy is arising with  $P_{yy}$  being larger than  $P_{xx}$  and  $P_{zz}$ .

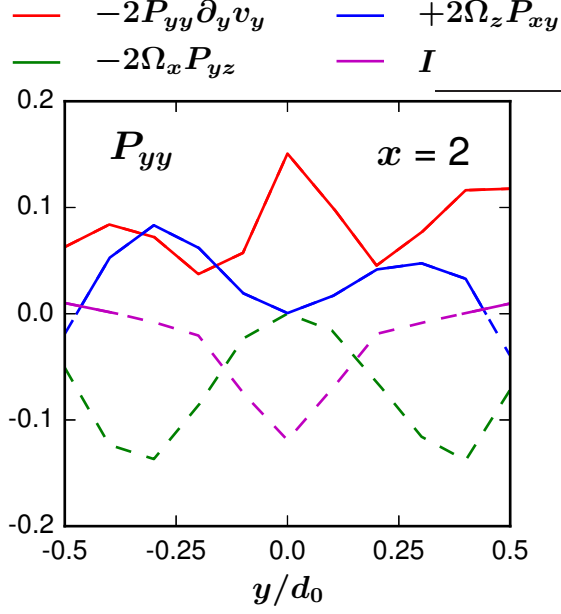


FIG. 2: Run B. Cut across the electron layer in  $Y$  direction (at  $X = 2 d_0$ ,  $t = 80 \Omega_0^{-1}$ ) for the terms defined in Eq. (7) for  $P_{yy}$ . For coloured lines, solid lines are used when the associated term increases the absolute value of pressure component, while dashed lines are used when this term decreases its absolute value.

One understands that the origin of the  $P_{yy}$  structure in the electron layer results from the component of  $[D_S]$  involving  $P_{yy}$  itself and gradient of the electron inflow velocity  $\partial_y V_y$ . The growth of  $P_{yy}$  by the  $[D_S]$  term is then self-fueled. Nonetheless, when we remove the isotropization term acting on  $P_{yy}$  in run C, it still doesn't diverge being limited by the term  $[D_A]$  (not shown here). Meaning the growth of  $P_{yy}$  in the electron layer is intrinsically non-diverging. The term  $[I]$  clearly acts in order to reduce the anisotropy.

Fig. 3 (a) shows the contribution of terms from Eq. (7) for  $P_{xx}$  in the electron layer. The isotropization term  $[I]$  is clearly dominant in the mid-plane  $Y = 0$ . While for  $P_{yy}$  the term  $[I]$  decreases  $P_{yy}$ , it increases  $P_{xx}$  and also  $P_{zz}$ , although not shown here. For all component considered, this highlights the isotropization nature of this term.

Now focusing on the separatrices, Fig. 1 (c) exhibits a clear structure of enhanced pressure on both sides of the separatrices for the  $P_{xx}$  component. It appears from panel (b) of Fig. 3 that this structure results from the term  $[C]$ . Above and below the separatrices,  $[C]$  involving  $P_{xy}$  makes  $P_{xx}$  to grow while  $[D_S]$  is not efficient enough at electron scale to limit the growth of  $P_{xx}$ .

As a partial conclusion, an electron layer is developing in the mid-plane because of the symmetric part of driver term for the  $P_{yy}$  component. The two other diagonal components are then affected by this growth because of

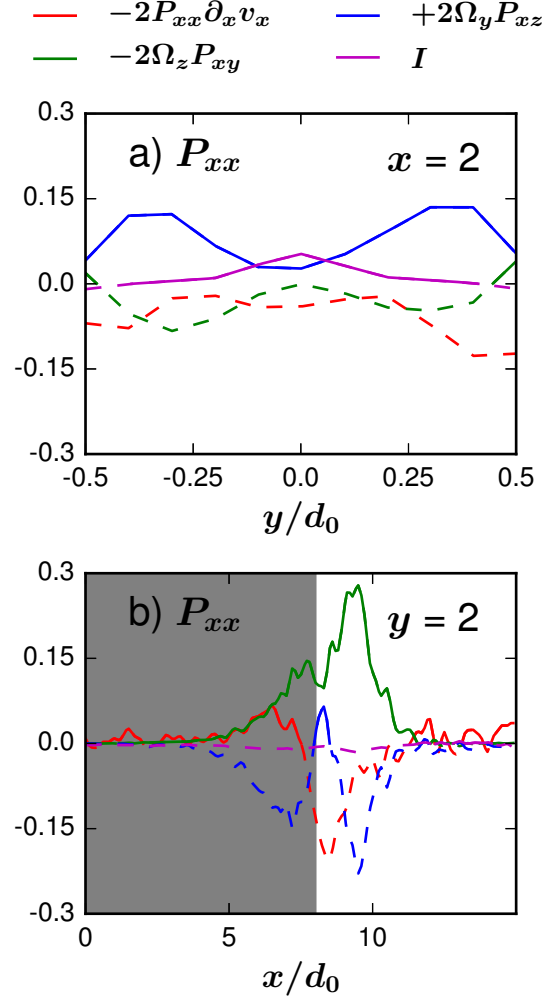


FIG. 3: Run B. Cuts for the terms defined in Eq. (7) for  $P_{xx}$  at  $t = 80 \Omega_0^{-1}$ : (a) crossing electron layer in  $Y$  direction (at  $X = 2 d_0$ ); (b) crossing separatrix in  $X$  direction (at  $Y = 2 d_0$ ), grey area represents above the separatrix region. The format for coloured lines is the same as in Fig. 2

the isotropization term. This growth is not numerically a problem, as it is limited whatever the  $\tau$  value in the isotropization term. The picture is quite different at the separatrices: the  $P_{xx}$  component is growing essentially because of the  $P_{xy}$  which acts through  $[C]$ . Without any isotropization of both  $P_{xx}$  and  $P_{xy}$  at the separatrices, these two components would diverge.

We then focus on the sources of the off-diagonal components of pressure tensor. Fig. 1 (d)-(f) displays the three off-diagonal components at  $t = 80 \Omega_0^{-1}$  for run B. The first important point is that the maximum values taken by the off-diagonal components of pressure tensor are about one order of magnitude smaller than those of the diagonal ones, as already pointed out by other studies of this kind<sup>19,21</sup>. The second point to notice is that the

patterns we observe are located in the electron layer and at the separatrices. The electron pressure agyrotropy is observed even where electrons are magnetized. Enhanced non-gyrotropy has been highlighted in separatrix regions in 2D fully kinetic simulations<sup>22</sup>, and can easily be understood as this region is precisely the topological boundary between the upstream (cold) and downstream (heated) electron populations.

Because of the very low values of the off-diagonal components of pressure tensor, the analysis of their origin is very sensitive to noise. We focus on the  $P_{xy}$  component as we will show that it is the important term, both in the electron layer (with physical consequences) and at the separatrices (with numerical issues). As a general structure,  $P_{xy}$  has a quadrupolar structure in the electron layer embedded in a second one of opposite polarity at the separatrices.

In the electron layer, as depicted on panel (a) of Fig. 4,  $P_{xy}$  is growing because of term  $[D_S]$  involving the  $P_{yy}$  component, and balanced by the term  $[C]$  involving anisotropy  $P_{xx} - P_{yy}$ . The growth of  $P_{xy}$  component in the electron layer is then a consequence of the growth of  $P_{yy}$  component, and is thus observed at the same scales. In the same way as for  $P_{yy}$ , this growth is bounded by the thickness of the electron layer because of the regularizing effect of the agyrotropic part of the term  $[C]$ .

We now focus on the structure of  $P_{xy}$  component at the separatrices. While not depicted, the effect of  $[D_C]$ ,  $[D_A]$  and  $[I]$  terms are very marginal, and the  $[D_S]$  and  $[C]$  terms seems to cancel each other out. But the structure at the separatrices is twofold : the value of  $P_{xy}$  is vanishing at the separatrices, but is observable at its inner and outer edges of the separatrices. On panel (b) of Fig. 4, using the same format as Fig. 3 (b), we observe that the agyrotropic component of the term  $[C]$  is there at play, as well as the term  $[D_S]$  involving  $P_{yy}$  component. Without any isotropization,  $P_{xy}$  component at the separatrix is growing up to unrealistic diverging values because of cyclotron term.

As a partial conclusion,  $P_{xy}$  is growing in the electron layer because of the driver, and is limited by the anisotropy  $P_{xx} - P_{yy}$ . There, no matter how weak the isotropization term is, these structures will not diverge. At the separatrices, the growth of  $P_{xy}$  is more sensitive as it results from the growth of  $P_{yy}$  (associated with the anisotropy), and agyrotropy involving  $P_{xz}$ , which in turn is growing because of the anisotropy  $P_{xx} - P_{zz}$ .

A general picture can now be drawn in the electron layer :

- a thin structure of enhanced value of  $P_{yy}$  is developing at electron scale in the very middle of the current sheet.
- this structure also develops for  $P_{xx}$  and  $P_{zz}$  because of the isotropization term.
- this resulting electron layer also exhibits a  $P_{xy}$  component developing as a direct consequence of the anisotropy  $P_{xx} - P_{yy}$ .

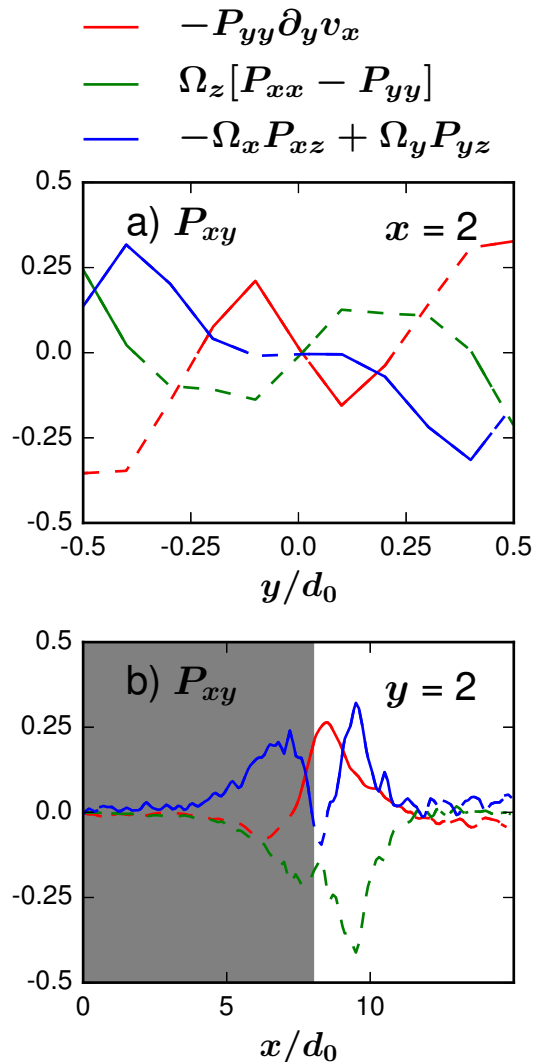


FIG. 4: Run B. Cuts for the terms defined in Eq. (7) for  $P_{xy}$  at  $t = 80 \Omega_0^{-1}$ : (a) crossing electron layer in  $Y$  direction (at  $X = 2 d_0$ ); (b) crossing separatrix in  $X$  direction (at  $Y = 2 d_0$ ), grey area represents above the separatrix region. The format for coloured lines is the same as in Fig. 2

as well as in the separatrices :

- the  $P_{xx}$  and  $P_{xy}$  components are mutually feeding one the other, essentially through the term  $[C]$ .
- if not limited by the isotropization term, these two components of the pressure tensor grow in a numerically unstable way.

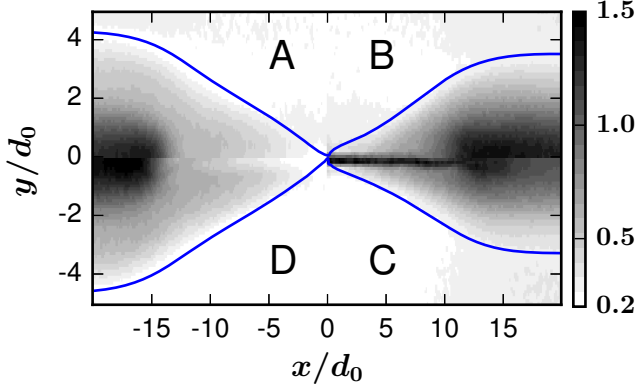


FIG. 5:  $P_{yy}$  at  $t = 80 \Omega_0^{-1}$  normalized to the initial maximum  $P_0 = n_0 k_B T_0$ .

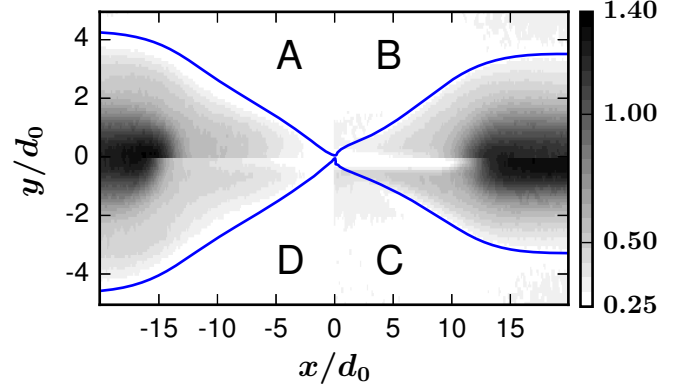


FIG. 6: Electron density at  $t = 80 \Omega_0^{-1}$  normalized to the initial maximum  $n_0$ .

## V. MACROSCOPIC CONSEQUENCES FOR THE CURRENT SHEET

As concluded in the previous section, the growth of  $P_{xx}$  (and the associated anisotropy  $P_{xx} - P_{zz}$ ) as well as the growth of  $P_{xy}$  at the separatrices are key points in the numerical stability of the system. The isotropization term modelling the role of electron heat flux divergence acts in a way to limit the growth of both  $P_{xx}$  and  $P_{xy}$ . Run C and D are intended to evaluate the consequences of the isotropization term efficiency on  $P_{xx}$  and  $P_{xy}$ .

The reason for run C is to evaluate how the problem evolves if the isotropization term only acts on  $P_{xx}$  and  $P_{xy}$  components. The reason for run D:  $P_{xy}$  happens to play a key role in the time evolution of both  $P_{xx}$  and  $P_{yy}$ . But the summation of the equations governing their time evolution cancels out the term involving  $P_{xy}$ , meaning that run D is the one where the destabilizing effect of  $P_{xy}$  is artificially removed.

In order to be able to clearly compare the results for runs A, B, C and D, we display the results for each of these runs in a given quadrant of the  $(x, y)$  space (taking advantage of the symmetry in both  $X$  and  $Y$  direction). Fig. 5 displays the  $P_{yy}$  component for these four runs. The electron layer is clearly visible in run B, and even more pronounced in run C with a longer extent in the  $X$  direction. But this pressure structure is totally missing in run D, meaning that the appearance of this electron layer critically depends on the growth of the  $P_{xy}$  component.

The  $P_{yy}$  structure can interestingly be compared to the density given in Fig. 6. For run B and even more clearly for run C, one observes a density gap in the electron layer, between the two density bulges downstream from the  $X$  point. We then need to investigate the  $Y$  component of the electric field (coming from the electron Ohm's law) in order to understand why the ions are expelled from the electron layer. The different terms of the Ohm's law are depicted in Fig. 7.

For run B, the  $E_y$  electric field has a very sharp bipolar

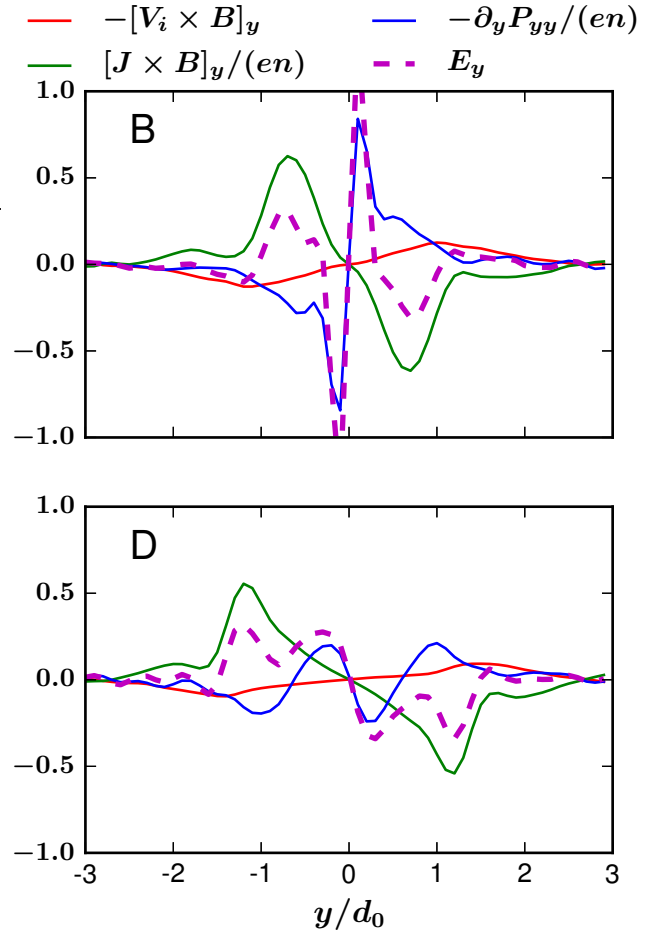


FIG. 7: Cut in  $Y$  direction at  $X = 4$  of the Ohm's law terms Eq. (2) for  $E_y$  component (averaged over 10 time steps for  $79.5 < t < 80.5$ ): run B with layer (upper panel), run D without layer (lower panel).

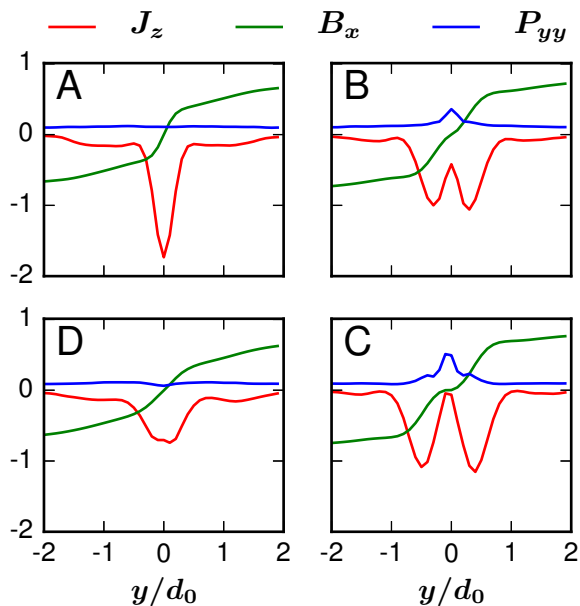


FIG. 8: Cut in  $Y$  direction at  $X = 0$  averaged over 5 time steps for  $67.8 < t < 68.2 \Omega_0^{-1}$ : out-of-plane current  $J_z$  (red), magnetic field  $B_x$  (green), diagonal pressure component  $P_{yy}$  (blue).

structure embedded in this electron layer which gets the particles out of the electron layer. This is the main difference with run D, where such a bipolar gradient pressure term exists, but with a smaller amplitude and an opposite direction. This electric field is mostly due to the gradient of  $P_{yy}$  component in  $Y$  direction, that is increased in the mid-plane representing the heated bouncing electrons. Inspecting the terms for the time evolution of  $P_{yy}$  displayed in Fig. 2, none of them is associated with any density gradients, meaning there is no mechanism which could limit the growth of  $P_{yy}$  and the associated density gap. Furthermore, these structures stay quite stationary, the ensuing pressure balance questions the associated magnetic structure.

Fig. 8 shows a cut through the X point for the out-of-plane current  $J_z$ . We observe for run A the standard pattern: the scalar pressure is somewhat constant through the current sheet and the reversal of magnetic field is quite sharp in the middle of the current sheet. As a consequence, the associated  $J_z$  current has a highly peaked structure.

For run B and C, the situation is quite different. Because of the increased  $P_{yy}$  pressure in the electron layer, by pressure balance the magnetic field inside the electron layer has a lower value compared to run A. In order to maintain this plateau in the magnetic field, the associated current  $J_z$  is also smaller at the very middle of the electron layer. This straightforwardly results in a bifurcated structure of the current sheet that we observe at sub-ion scale. The minimum of current in the mid-plane is even more pronounced for run C, which outlines the

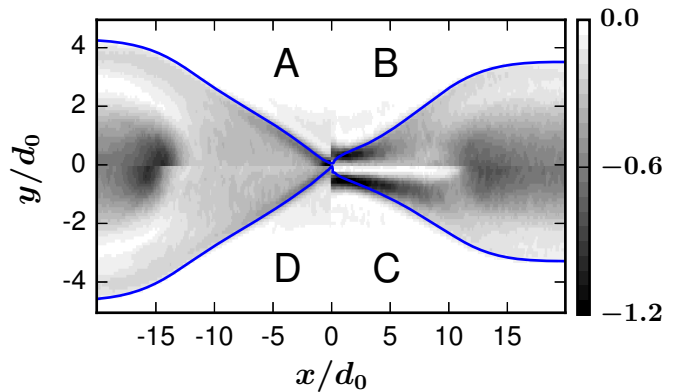


FIG. 9: Color-coded value of the  $J_z$  component of the total current at  $t = 80 \Omega_0^{-1}$ , for runs A (top left), B (top right), C (lower right) and D (lower left). The separatrices are depicted in blue line.

clear role of the development of  $P_{xx} - P_{yy}$  anisotropy and  $P_{xy}$  agyrotropy. This conclusion is consolidated by run D, where the current sheet is no more bifurcated, remembering that this run is the one where these two terms are artificially quenched.

Fig. 9 displays the two-dimensional spatial configuration of the  $J_z$  component of the total current. As commonly observed in 2D reconnection studies, for run A and D the thickness of the out-of plane current sheet is diminished close to the X point, and advected downstream. The picture is quite different for run B and C: this current is totally vanishing at  $Y = 0$ , but expelled above and below the mid-plane, resulting in a bifurcated current sheet. Such a bifurcated current sheet (BCS) has already been discussed theoretically<sup>23</sup>, numerically<sup>24</sup> and with in-situ data observations<sup>25</sup>. Observed numerically<sup>20,26,27</sup> BCSs were carried by non-gyrotropic electron pressure, associated with anisotropic heating, due to electrons heated in the direction perpendicular to the magnetic field.

On the numerical side using 2D fully kinetic simulations one obtains an extended current layer<sup>28</sup>, which thickness decreases approaching the realistic ion to electron mass ratio. Furthermore, a structure of the  $J_z$  current at electron scale can be observed<sup>29</sup> because of dependence on the mass ratio. Out from the reconnection context, BCS have also been reported, associated with the Low-Hybrid-Drift-Instability developing in the current sheet<sup>26</sup> and have been suggested to be a tropism of current sheet<sup>30</sup>. It is suggested<sup>20</sup> that the BCS scale depends on the electron bounce width, which depends on the thickness of current sheet and the electron mass. They hence clearly observe a decrease of BCS size when going to realistic electron mass, but it is still observed at this limit. As the tearing mode is suggested to be more unstable<sup>27</sup>, this gives no insight about the efficiency of the reconnection process. On the observation side, while

many in-situ observation of BCS have been reported at ion scale<sup>31–33</sup>, a recent study also reported the observations of BCS at electron scale<sup>34</sup>.

While BCS are not always observed numerically<sup>28,35</sup>, the electron mass greatly influences the current sheet structure. As known, increasing ion to electron mass ratio up to realistic values requires significant reduction of resolution. In the scope of the work to keep the same spatial and temporal resolution we have performed B-type run with a decreased mass ratio  $\mu=10$ . The distance between peaks of the out-of-plane current slightly increases while the absolute minimum depth in the mid-plane becomes less pronounced. From what we expect that increasing ion to electron mass ratio results in smaller peak separation and the out-of-plane current in the mid-plane should be exact zero. But investigation of mass ratio dependence is out of scope of this paper, and need further analysis.

It is also important to note the  $X$ -extent of BCS, on the order of 5 ion inertial lengths for run B. It is even larger (about  $10 d_0$ ) for run C, which supports the fact that the enhanced value of  $P_{yy}$  in the electron layer (not isotropized in run C) is on the origin of this structure. The problems of physical mechanism for electrons cooling in the mid-plane and heat flux closure are still unclear for hybrid models with pressure tensor evolution, and need for future detailed comparisons with fully kinetic simulations to better understand and better model the differences that we observe.

## VI. CONSEQUENCES FOR THE RECONNECTION RATE

Fig. 10 displays the time evolution of reconnection rate. It is computed as the local value of the out-of-plane electric field  $E_z$  at the X point, normalized to the upstream magnetic field and Alfvén velocity, at  $X = 0$  and  $Y = 6d_0$ . As classically observed in numerical studies of magnetic reconnection<sup>5</sup>, the reconnection rate grows from zero during a transient phase, and then reaches a constant value hence outlining the stationarity of reconnection process. This value is close to 0.1 for run A and D, 0.08 for run B and 0.06 for run C. While not spectacular, these differences are noticeable, and show that the time integration of the six-component electron pressure tensor results in a decrease of the reconnection process efficiency. These features are in agreement with the fact that for run B and C, the opening angle of the separatrices is smaller than for run A and D (see Fig. 5, 6 and 9).

On Fig. 11, we display the  $E_z$  component of the electric field (thick red dashed line) depending on  $Y$  position for a cut at  $X = 0$ . Each term of the Ohm's law are depicted in color, including the two electron pressure terms associated with their agyrotropy. One observes the classical pattern for run A : in the MHD region, where ions are magnetized ( $y > 2d_0$ ), the electric field is mainly due

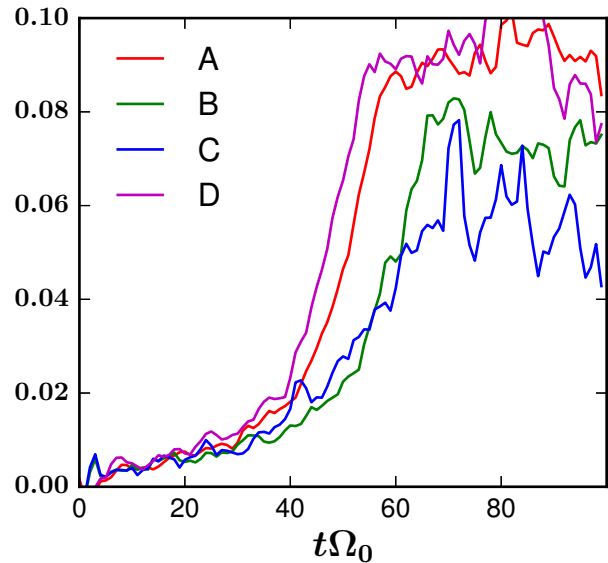


FIG. 10:  $E_z$  component of the electric field at X-point, normalized to the upstream magnetic field and Alfvén velocity : red, green, blue and magenta are for runs A, B, C and D, respectively.

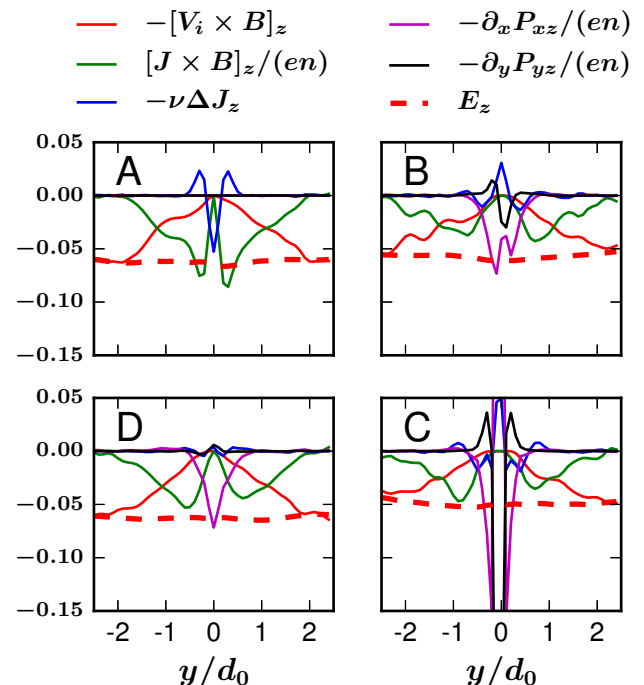


FIG. 11: Cut in  $Y$  direction at  $X = 0$  of the Ohm's law terms Eq. (2) for  $E_z$  component (averaged over 10 consecutive steps for  $79.5 < t < 80.5$ ).

to the ideal term associated with the inward advection of plasma in the reconnection region. Closer to the field reversal, the dominant term is the Hall term, associated with the main  $B_x$  component of the magnetic field and current  $J_y$ . In the very middle of the current sheet, as  $B_x$  vanishes, the hyper-viscous dissipative term is the only one at play, this one being restricted to few grid points. The case of run D is quite similar, except that the Hall term has a smaller amplitude. Furthermore, the pressure term associated with  $P_{xz}$  is the leading one in the middle of current sheet, the hyper-viscous one being negligible. This results from the modified structure of the  $J_z$  current and the associated smaller value of its laplacian.

The cases of runs B and C are quite different from A. In Fig. 11, while dominating in the MHD region, the ideal term is less important as the ion velocity is smaller than in classical case A. A possible mechanism for the reconnection rate reduction is the drag force already discussed by Yin et al.<sup>21</sup>, acting on ions entering the near-X-point region. This drag force could result from the pressure gradient in inflow direction. In Fig. 7 the bi-polar  $E_y$  component of the electric field in the very middle of the electron layer is directed outward from the mid-plane, and results from the strong pressure gradient of  $P_{yy}$  component. A rough estimation of the energy wall associated with this localized electric field is 0.1, that is comparable to the initial kinetic energy of the thermal ions. While the reconnection rate is believed to be determined by ion scale processes, such a highly localized electrostatic field could significantly slow-down the ions convecting through the X-point region. Because of low plasma compressibility we see also a net reduction of ideal term for the reconnection electric field for runs B and C in Fig. 11. Looking back at Fig. 6 we can find an excess of dragged plasma density under and above the X-point region for runs B and C comparing with A and D.

Closer to the mid-plane for run B, the reconnection electric field is dominated by the electron pressure term associated with  $P_{xz}$ . The electron pressure term associated with  $P_{yz}$  is also at play, while less important. This pattern is also observable for run C, but as  $P_{xz}$  and  $P_{yz}$  components are not isotropized, the contribution of these terms for  $E_z$  is larger. As the hyper-viscous term is an indicator of current curvature, one should also notice the term for runs B and C, which has a sign opposite to the one observed in run A. As already pointed out, its form results from the bifurcated nature of the out-of-plane current having absolute minimum in the mid-plane and maximum on its edges.

As partial conclusion of this section we stress that the reconnection rates reach higher values for runs without electron layer (A and D) than for runs exhibiting an electron layer (B and C). The possible mechanism for smaller out-of-plane electric field is the strongly localized electrostatic field in the mid-plane because of the pressure gradient that slows down the ions convection. The pressure anisotropy in the mid-plane develops because of  $P_{yy}$  component, tuning the isotropization on that component

could reduce the electrostatic field and as result the bifurcation of the out-of-plane current.

## VII. CONCLUSION

We studied how the time integration of electron pressure tensor can be considered in a hybrid code where electrons are treated as a fluid. Aside from an existing implicit method to integrate the fast electron cyclotron part of this tensor, we propose an explicit method based on subcycling. We put forward that such method converges to the same results as the one obtained with the implicit method, but saving about 30% of the total computational time. We also outlined the requirement of an isotropization term of this tensor (both diagonal and non-diagonal components) in order to restrain the growth of some of these components, located at the separatrices. Such isotropization is physically associated with the divergence of the electron heat flux. While this term is numerically sensitive to handle, several approximations have been proposed to model it correctly. Such approach is mandatory as the time integration of the exact equation for high order moment (larger than 3) is numerically unstable and introduce eigenmodes physically not justified. We also show that the  $P_{xx}$  and  $P_{xy}$  components of the electron pressure tensor are the only ones that need to be isotropized (in Harris-type sheet models) in order to limit the growth of unstable structures at the separatrices.

We put forward the existence of two characteristic structures in the development of magnetic reconnection in a modified Harris sheet initially pinched : an electron layer at electron scale close to the mid-plane where the diagonal pressure tensor component (dominated by the  $P_{yy}$  component) is increased, and an increase of the  $P_{xx}$  component at separatrices. These structures are also associated with more complex patterns for the off-diagonal components of electron pressure tensor. The structures at the separatrices are the most sensitive as their isotropization is mandatory for the stability of calculations. More precisely,  $P_{xx}$  and  $P_{xy}$  are the components which growth needs to be limited. We show that the  $P_{yy}$  structure in the electron layer is associated with an outward  $E_y$  electric field, which results in a drag force, acting on ions entering the reconnection region. By force balance, the magnetic field also decreases in the electron layer, which is associated with the splitting of the current sheet. As a consequence, the Hall component of the reconnection electric field is decreased. A clear and direct consequence is that the associated reconnection rate is smaller than in the case of isothermal closure for electrons where such electron layer is not developing.

We performed this study using ion to electron mass ratio  $\mu = 100$ , which is one order of magnitude smaller than the realistic one. Unfortunately, in hybrid simulations decrease the  $\mu$  value would necessitate a smaller grid size, which is resource consuming in CPU time because

of the quadratic relation between time step and grid size. Nonetheless, we conjecture that increasing the mass ratio up to the realistic value would decrease the thickness of the electron layer, and hence increase the gradient of the  $P_{yy}$  component. The  $E_y$  component of the electric field would then increase, slowing ions on entering the reconnection region.

## VIII. ACKNOWLEDGMENTS

The research was supported by the Ministry of Science and Higher Education of the Russian Federation, state assignment for the Institute of Applied Physics RAS, project 0035-2019-0012. The simulations were partially performed on resources provided by the Joint Supercomputer Center of the Russian Academy of Sciences.

## IX. DATA AVAILABILITY

The data that support the findings of this study are available from the corresponding author upon reasonable request.

- <sup>1</sup>J. Taylor, *Reviews of Modern Physics* **58**, 741 (1986).
- <sup>2</sup>J. W. Dungey, *Physical Review Letters* **6**, 47 (1961).
- <sup>3</sup>E. d. G. Dal Pino, P. Piovezan, and L. Kadowaki, *Astronomy & Astrophysics* **518**, A5 (2010).
- <sup>4</sup>W. Wan and G. Lapenta, *Physics of Plasmas* **15**, 102302 (2008).
- <sup>5</sup>J. Birn, J. Drake, M. Shay, B. Rogers, R. Denton, M. Hesse, M. Kuznetsova, Z. Ma, A. Bhattacharjee, A. Otto, et al., *Journal of Geophysical Research: Space Physics* **106**, 3715 (2001).
- <sup>6</sup>M. Hesse, T. Neukirch, K. Schindler, M. Kuznetsova, and S. Zenitani, *Space Science Reviews* **160**, 3 (2011).
- <sup>7</sup>V. M. Vasyliunas, *Reviews of Geophysics* **13**, 303 (1975).
- <sup>8</sup>M. M. Kuznetsova, M. Hesse, and D. Winske, *Journal of Geophysical Research: Space Physics* **103**, 199 (1998).
- <sup>9</sup>M. A. Shay, J. F. Drake, R. E. Denton, and D. Biskamp, *Journal of Geophysical Research: Space Physics* **103**, 9165 (1998).
- <sup>10</sup>W. Daughton and H. Karimabadi, *Physics of Plasmas* **14**, 072303 (2007).
- <sup>11</sup>D. Winske and M. Hesse, *Physica D Nonlinear Phenomena* **77**, 268 (1994).
- <sup>12</sup>M. Hesse, D. Winske, and M. M. Kuznetsova, *Journal of Geophysical Research: Space Physics* **100**, 21815 (1995).
- <sup>13</sup>R. Smets, G. Belmont, N. Aunai, and L. Rezeau, *Physics of Plasmas* **18**, 102310 (2011).
- <sup>14</sup>D. Winske and K. Quest, *Journal of Geophysical Research: Space Physics* **91**, 8789 (1986).
- <sup>15</sup>J. P. Boris and R. A. Shanny, *Proceedings: Fourth Conference on Numerical Simulation of Plasmas, November 2, 3, 1970* (Naval Research Laboratory, 1972).
- <sup>16</sup>E. Harris, *Nuovo Cimento* **23**, 115 (1962).
- <sup>17</sup>S. Zenitani, M. Hesse, A. Klimas, C. Black, and M. Kuznetsova, *Physics of Plasmas* **18**, 122108 (2011).
- <sup>18</sup>G. W. Hammett and F. W. Perkins, *Physical Review Letters* **64**, 3019 (1990).
- <sup>19</sup>L. Wang, A. H. Hakim, A. Bhattacharjee, and K. Germaschewski, *Physics of Plasmas* **22**, 012108 (2015).
- <sup>20</sup>Y.-H. Liu, J. Birn, W. Daughton, M. Hesse, and K. Schindler, *Journal of Geophysical Research: Space Physics* **119**, 9773 (2014).
- <sup>21</sup>L. Yin, D. Winske, S. Gary, and J. Birn, *Journal of Geophysical Research: Space Physics* **106**, 10761 (2001).
- <sup>22</sup>J. Scudder and W. Daughton, *Journal of Geophysical Research: Space Physics* **113** (2008).
- <sup>23</sup>L. M. Zelenyi, H. V. Malova, and V. Y. Popov, *Soviet Journal of Experimental and Theoretical Physics Letters* **78**, 296 (2003).
- <sup>24</sup>D. Delcourt, H. Malova, and L. Zelenyi, *Journal of Geophysical Research: Space Physics* **109** (2004).
- <sup>25</sup>A. Runov, R. Nakamura, W. Baumjohann, T. Zhang, M. Volwerk, H.-U. Eichelberger, and A. Balogh, *Geophysical Research Letters* **30** (2003).
- <sup>26</sup>W. Daughton, G. Lapenta, and P. Ricci, *Physical Review Letters* **93**, 105004 (2004).
- <sup>27</sup>T. Matsui and W. Daughton, *Physics of Plasmas* **15**, 012901 (2008).
- <sup>28</sup>M. A. Shay, J. F. Drake, and M. Swisdak, *Phys. Rev. Lett.* **99**, 155002 (2007).
- <sup>29</sup>J. Drake, M. Shay, and M. Swisdak, *Physics of Plasmas* **15**, 042306 (2008).
- <sup>30</sup>H. Karimabadi, W. Daughton, and K. B. Quest, *Journal of Geophysical Research: Space Physics* **110** (2005).
- <sup>31</sup>M. Hoshino, T. Yamamoto, T. Mukai, A. Nishida, and S. Kokubun, *Advances in Space Research* **18**, 5 (1996).
- <sup>32</sup>Y. Asano, R. Nakamura, W. Baumjohann, A. Runov, Z. Vörös, M. Volwerk, T. Zhang, A. Balogh, B. Klecker, and H. Reme, *Geophysical Research Letters* **32** (2005).
- <sup>33</sup>A. Runov, V. Sergeev, R. Nakamura, W. Baumjohann, S. Ap-atenkov, Y. Asano, T. Takada, M. Volwerk, Z. Vörös, T. Zhang, et al., in *Annales Geophysicae* (2006), vol. 24, pp. 247–262.
- <sup>34</sup>C. Norgren, D. B. Graham, Y. V. Khotyaintsev, M. André, A. Vaivads, M. Hesse, E. Eriksson, P.-A. Lindqvist, B. Lavraud, J. Burch, et al., *Journal of Geophysical Research: Space Physics* **123**, 9222 (2018).
- <sup>35</sup>M. Hesse, J. Birn, and M. Kuznetsova, *Journal of Geophysical Research: Space Physics* **106**, 3721 (2001).